ELSEVIER

Contents lists available at ScienceDirect

Journal of Environmental Chemical Engineering

journal homepage: www.elsevier.com/locate/jece



Performance evaluation of novel Ca/Mn-doped perovskite as a multifunctional material in chemical looping reverse water gas shift process for low-carbon fuels

Adnan Akhtar^a, Adam Zaidi^b, Christopher de Leeuwe^c, Angelos M. Efstathiou^d, Anam Asghar^e, Mohamed G. Hassan-Sayed^a, Syed Zaheer Abbas^{a,*}

- ^a School of Chemistry and Chemical Engineering, University of Southampton, University Road, Southampton SO17 1BJ, United Kingdom
- b Department of Chemical Engineering, The University of Manchester, Booth St E, Manchester M13 9PL, United Kingdom
- ^c Department of Chemical Engineering, University of Bath, Claverton Down, Bath BA2 7AY, United Kingdom
- d Department of Chemistry, Heterogeneous Catalysis Laboratory, University of Cyprus, 1 University Avenue, University Campus, Nicosia 2109, Cyprus
- e Instrumental Analytical Chemistry, Faculty of Chemistry, University of Duisburg-Essen, Universitätsstr. 5, Essen, Germany

ARTICLE INFO

Keywords: Calcium doping Chemical looping CO₂ utilization Perovskite Reverse water gas shift Syngas

ABSTRACT

The chemical looping reverse water gas shift (CL-RWGS) catalytic process offers a promising approach for decarbonizing energy-intensive industries. The CL-RWGS promotes the formation of surface oxygen vacancies in the material, which are subsequently replenished by extracting oxygen from CO2, resulting in syngas production. However, there remains a significant gap in the development of materials that not only exhibit redox activity but also enable in-situ carbonation, offering dual functionality for enhanced CO2 utilization. This study introduces a novel calcium- and manganese-doped LaNiO $_3$ perovskite, designed for integrated CO $_2$ sorption and in-situ utilization during CL-RWGS process. Comprehensive characterization confirmed the material's crystalline structure, porosity, and successful incorporation of Ca and Mn dopants. Thermogravimetric analysis (TGA) across 700 - 900 °C revealed a peak oxygen storage capacity of 1.97 mmol O₂/g and demonstrated excellent redox stability, with less than 1 % performance loss over 17 cycles. RWGS experiments conducted in a packed bed reactor demonstrated up to 57 % CO₂ to CO conversion at 900 °C, approaching the thermodynamic equilibrium value of 60% under the same operating conditions. Moreover, an H_2/CO molar ratio of ~ 2.0 , suitable for Fischer-Tropsch synthesis, was achieved at 600 °C and 1.0 bar with a feed H2/CO2 molar ratio of 1.0, attributed to CO2 chemisorption via a carbonation-driven mechanism facilitated by the presence of CaO phase. These results suggest that the calcium- and manganese-doped LaNiO3 perovskite is a highly promising multi-functional material for chemical looping-based CO2 utilization technologies.

1. Introduction

Energy-intensive industries account for 10 Gt of global CO_2 emissions annually and pose a significant challenge to achieving net-zero emissions by 2050, primarily due to their dependence on high-temperature processes and carbon–intensive feedstocks [1]. Carbon Capture and Utilization (CCU) has emerged as a promising approach for decarbonizing such sectors, however, its large-scale application remains limited by the high energy requirements for CO_2 purification and the risk of leakage during transportation [2].

Integrated Carbon Capture and Utilization (ICCU) provides a more energy-efficient solution by combining CO_2 adsorption and catalytic

conversion within a singular process unit, thereby minimizing energy losses and enhancing total process efficiency [3]. One of the most promising approaches in ICCU involves the use of dual functional materials (DFMs), which typically combine CO₂ sorbents, such as Na-, K-, Mg- and Ca-based oxides, with a CO₂ conversion catalyst based on transition metals, such as Ni, Cu, or Ru [4–6]. However, the effectiveness and stability of DFMs in ICCU processes, such as CO₂ methanation, dry reforming of CH₄, and Fischer-Tropsch synthesis (FTS), are often limited by carbon deposition [7–9]. To address this challenge, integrating DFMs with oxygen storage and release (OSR) materials has been proposed as an effective strategy to mitigate carbon deposition and enhance CO₂ conversion [10]. Among several approaches, chemical looping (CL) has

E-mail address: s.z.abbas@soton.ac.uk (S.Z. Abbas).

^{*} Corresponding author.

emerged as a promising ICCU strategy due to its relatively low energy requirements and economic viability. In a typical CL-based ICCU process employing both OSR and DFM materials, CO_2 is first adsorbed by the sorbent and subsequently converted into syngas via CH_4 reforming [11]. The OSR material facilitates lattice oxygen transfer for partial oxidation of CH_4 and is regenerated with air through an exothermic reaction, providing the heat necessary for the endothermic reforming step [12]. Therefore, a single multifunctional material that combines redox capability with CO_2 sorption functionality could offer a more efficient and technically robust CL-based ICCU process, enabling higher product purity within a single reactor.

In this context, perovskite materials have gained considerable attention due to their wide range of applications in various advanced technologies [13-15]. Particularly in CL processes, perovskites have been recognized as promising OSR materials due to their structural flexibility and redox tunability [16-18]. The generic formula of perovskite, ABO3, consists of an A-site occupied by alkali or alkaline earth metal, and a B-site containing transition metal such as Ni, Cu, Fe, or Co [19]. This structural versatility allows substitution at the A- and B- sites, enabling the formation of oxygen vacancies that enhance OSR properties during redox reactions. LaNiO3, a well-known perovskite, has been extensively applied in ICCU applications, including CO₂ methanation via the Sabatier reaction [20], and as a DFM when integrated with CeO₂ for CO₂ adsorption and *in-situ* conversion [21,22]. It has also shown promise in hybrid plasma-catalysis systems, such as dielectric barrier discharge configurations [23]. In CL applications, LaNiO3 is favoured for its high selectivity and thermal stability, particularly in steam reforming of ethanol for hydrogen production [24]. Various modifications of pristine LaNiO₃ with elements such as Ti, Cu, and Co have been explored to further improve its performance in chemical looping combustion (CLC) and partial oxidation reactions [25-27]. However, to the best of authors' knowledge, no single perovskite material has been reported that simultaneously exhibits both OSR and DFM functionalities. Furthermore, LaNiO3-based materials have yet to be investigated within the framework of chemical looping integrated with the reverse water gas shift (CL-RWGS) reaction process. The RWGS process is a well-established reaction pathway for converting CO₂ into CO, a key intermediate for syngas production via H₂ utilization [28,29]. The main reactions involved in the three-step CL-RWGS process using perovskites are summarized in Table 1. This three-step process offers several advantages as air oxidation fully regenerates the perovskite, preventing the accumulation of oxygen vacancies and ensuring stable CO yield. Complete re-oxidation also preserves the structural integrity of the perovskite by restoring its lattice structure and avoiding any phase segregation [30]. Additionally, since air oxidation of perovskite is exothermic [31], the heat released can be utilized in the subsequent RWGS cycle, thus enhancing the overall energy efficiency of the process. A detailed schematic illustration of CL-RWGS process in a packed bed reactor is also presented in Fig. 1 involving a conventional ABO3 perovskite, highlighting the air oxidation and RWGS stages.

In this study, LaNiO $_3$ perovskite was co-doped with Ca and Mn to assess its potential as a hybrid DFM-OSR material for ICCU applications. The incorporation of Ca was intended to enhance CO $_2$ sorption capacity due to its high basicity and well-known affinity for CO $_2$ [32]. Mn was

Table 1Key chemical reactions in a three-step CL-RWGS process using perovskites.

Stage	Reaction steps	Reaction	Nature of Reaction
Air oxidation	Oxidation	$ABO_{3\text{-}\gamma} + \frac{*\gamma}{2}O_2 \to ABO_3$	Exothermic ($\Delta H_{298 \text{ K}} < 0$)
RWGS	Reduction	$ABO_3 + \delta H_2 \rightarrow ABO_{3-\delta} + \delta H_2O$	Endothermic $(\Delta H_{298 \text{ K}} = 41.2 \text{ kJ/})$
	CO ₂ splitting	ABO _{3-δ} + (δ-γ) CO ₂ \rightarrow ABO _{3-γ} + (δ-γ) CO	mol)

^{*} γ denotes partial oxygen storage (0 $<\gamma<\delta$)

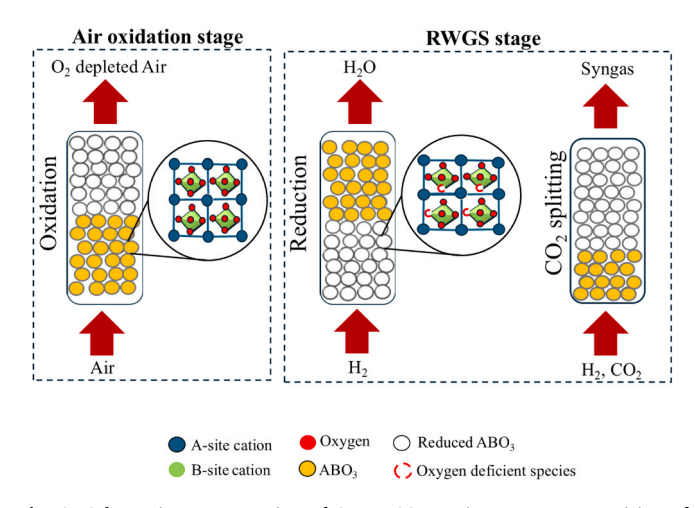


Fig. 1. Schematic representation of CL-RWGS reaction process comprising of air oxidation stage and RWGS stage.

introduced to promote the formation of oxygen vacancies and improve structural stability by reducing sintering and carbon deposition [33]. Furthermore, Mn has been reported to enhance the dispersion of Ni metal on the perovskite surface, thereby improving catalytic performance [34].

2. Materials and methods

2.1. Synthesis of metal doped perovskite materials

Ca- and Mn-doped LaNiO₃ perovskite samples (denoted as CLMN), with varying dopant loadings (wt%), were synthesized using a two-step procedure: (i) preparation of LaNiO₃ perovskite via the sol-gel method, and (ii) doping of Ca and Mn onto the as-prepared LaNiO₃ using the citrate method followed by calcination at 800 °C. To synthesize 5 g of LaNiO₃, 13.97 g of La (CH₃COO)₃·1.5 H₂O (99.9 %, Thermo Scientific Ltd., UK), 5.07 g of Ni (CH₃COO)₂.4H₂O (99 %, Thermo Scientific Ltd., UK), and 3.91 g of citric acid (99.8 %, Fischer Scientific Ltd., UK) were dissolved in a mixed solvent of ethanol and water (4:1 v/v). The resulting solution was sonicated for 1 h to ensure complete homogeneity, then stirred at 70 °C on a hot plate until a gel was formed. The gel was dried at 120 °C for 24 h to remove water and promote polyesterification. The dried product was subsequently calcined at 800 °C (ramp rate of 1 °C/min) for 24 h in a Carbolite® furnace, yielding a black LaNiO₃ powder.

In the second step, CaCO3 (99 % purity, Acros Ltd., UK) was dissolved in acetic acid to form calcium acetate. The resulting solution was added to a mixture containing Mn (CH₃COO)₂.4H₂O, citric acid, and the as-prepared perovskite powder in deionized water. The quantities of Ca and Mn precursors, along with citric acid (3.01 - 3.33 g), were adjusted to achieve the desired dopant loadings of 5, 10, and 15 wt% for each element. The mixture was sonicated for 1 h, followed by continuous stirring at 90 °C for 3 h. After the solution thickened, it was dried at 120 °C for 24 h and subsequently calcined at 800 °C (ramp rate of 1 °C/min) for 24 h. This step facilitated the diffusion of Ca and Mn ions into the LaNiO₃ lattice, promoting successful dopant substitution within the perovskite structure [35]. The resulting samples were designated CLMN-1 $(Ca_{0.15}La_{0.85}Mn_{0.05}Ni_{0.95}O_3),$ CLMN-2 (Ca_{0.2}L $a_{0.8}Mn_{0.1}Ni_{0.9}O_3$), and CLMN-3 ($Ca_{0.25}La_{0.75}Mn_{0.15}Ni_{0.85}O_3$) respectively, corresponding to the theoretical Ca- and Mn loading levels.

2.2. Characterization of materials - crystallinity, texture and morphology

Powder X-ray diffraction (XRD) was used to examine the crystalline structure of LaNiO $_3$ and all CLMN samples using a Bruker D2

Diffractometer with Cu K α radiation (λ = 1.54 Å). The XRD data were collected over diffraction angles (2 θ) from 20 to 80° at a scan rate of 1.2° /min. Surface morphology was analysed using a scanning electron microscope (SEM, Zeiss Gemini Sigma 500 VP, UK), with the samples affixed to carbon adhesive tapes. Elemental distribution of CLMN samples was evaluated by energy dispersive X-ray spectroscopy (EDX). To further quantify Ca and Mn concentrations in the CLMN samples, inductively coupled plasma-optical emission spectrometry (ICP-OES, Agilent 5800) was conducted. 12 mg of each sample was digested in10 mL of 0.5 M HNO3 solution, filtered, and diluted to 1000 mL prior to ICP-OES analysis. The BET specific surface area (m²/g) and cumulative pore volume (cm³/g) were determined using N2 adsorption-desorption isotherms at 77 K using Micromeritics II 3020 analyser. Before measurements, 0.3 g of each sample was degassed under vacuum at 120 °C for 4 h.

Transmission Electron Microscopy (TEM, Hitachi HT7700, 100 kV) was employed to assess particle size distribution and agglomeration following metal loading and calcination procedures. For TEM analysis, fine powder samples were dispersed in ethanol (10 mL), and 5 μL of suspension was deposited onto a carbon-coated grid and allowed to dry prior to imaging.

2.3. Oxygen storage properties

The oxygen storage capacity and stability of Ca- and Mn-doped LaNiO₃ samples were evaluated by thermogravimetric analysis (TGA) using a NETZSCH STA 449 F1 Jupiter analyser. TGA was performed to assess the oxygen release behaviour and thermal stability of the materials for CL applications. 50 mg of each sample was placed in an alumina crucible and subjected to consecutive reduction-oxidation cycles at temperatures ranging from 700 to 900 $^{\circ}\text{C}$ in 50 $^{\circ}\text{C}$ intervals, with heating rate of 10 $^{\circ}$ C/min. The reduction step was carried out using 4 H₂ in N₂ at the total flowrate of 250 mL/min, while oxidation was conducted with synthetic air at a flowrate of 200 mL/min. Reduction was maintained for 10 min, with the major weight loss occurring within the first 5 min, after which the rate gradually decreased until stabilization [36]. Oxidation was performed for 4 min, as OSR materials typically reoxidize within a short time frame. Between each redox cycle, N2 gas was used to purge the reactor to prevent direct contact between H2 and O2 gases. Each sample underwent 17 consecutive redox cycles, including two initial activation cycles. The oxygen storage capacity for each reduction cycle was calculated using Eq. 1:

$$R_o(\%) = \frac{m_o - m_r}{m_o} \times 100 \tag{1}$$

where R_o (wt.%) represents the oxygen storage capacity for each cycle, and m_o and m_r are the masses of the sample before and after reduction, respectively. Specific values of oxygen storage capacity (mmol O_2/g_{OSR}) were obtained by dividing R_o by the molar mass of O_2 (g/mol) and multiplying by 1000. Prior to the redox experiments, a blank run was performed using an empty crucible under identical conditions to record any mass changes not related to the samples. Additionally, a pre-oxidation step was carried out for each sample to remove volatile components and moisture absorbed during synthesis [37].

2.4. Reactor setup for CL-RWGS and calcium looping experiments

The CL-RWGS and calcium looping (CaL) experiments were conducted using a packed bed reactor setup, as described by Zaidi et al. [38]. The reactor consisted of a quartz silica tube (L×OD×WT: 550 mm \times 13 mm \times 2 mm) placed inside a Carbolite Gero® furnace. A total of 1.0 g of CLMN material (particle size: 310 - 720 μm) was loaded, forming a bed length of \sim 3.5 cm. Quartz wool was packed at both ends of the bed to hold CLMN material in place, ensuring uniform preheating of feed gases and consistent radial gas distribution within the reaction

Before the experimental campaign, the mass spectrometer was calibrated using standard gas mixtures passed through the reactor at ambient temperature. The recorded signals were used to normalize gas concentrations during analysis. CaL tests were first conducted in the packed bed reactor to assess the CO_2 sorption capacity of the material. Carbonation was carried out at $600\,^{\circ}C$ using a gas mixture containing $20\,$ vol% CO_2 , $10\,$ vol% He as a tracer gas, and $70\,$ N $_2$ at a constant gas hourly space velocity (GHSV) of $5000\,$ h $^{-1}$. The introduction of He gas alongside CO_2 served as a non-adsorbing internal standard, facilitating precise measurement of CO_2 exposure during the carbonation step. The appearance of He gas in the effluent stream marked the start of the carbonation phase. Reaction time measurements started (t = 0) when the He signal was first detected by mass spectrometer. The calcination stage was performed at $900\,^{\circ}C$ in a pure N_2 atmosphere to regenerate CLMN material.

For the CL-RWGS experiments, the operating conditions are summarized in Table 2. Prior to testing, the material was activated via redox cycling between 600 – 900 °C using 20 $\rm H_2$ and 10 $\rm O_2$ in He/N $_2$ mixtures for the reduction and oxidation steps, respectively. This activation step promoted uniform distribution of transition metals within the perovskite lattice and ensured reproducible performance. A GHSV of 5000 $\rm h^{-1}$ was maintained throughout the experiments to provide sufficient residence time for gas–solid reactions under high temperature conditions [39,40].

3. Results and discussion

3.1. Characterization of perovskite materials

3.1.1. Morphological, elemental and surface texture analysis

The morphology of LaNiO $_3$ and CLMN samples was examined using SEM, and the corresponding micrographs are presented in Fig. 2. As shown in Fig. 2a-b, LaNiO $_3$ exhibits a rod-like morphology, whereas the SEM images of CLMN-2 (Fig. 2c, d) show a granular structure, indicating a notable morphological transformation upon Ca and Mn doping. This transition from rod-like to granular morphology suggests that dopant incorporation significantly influenced the crystal growth behaviour of LaNiO $_3$. Furthermore, higher magnification images indicate the presence of porous structures in both LaNiO $_3$ and CLMN samples. This morphological observation is further supported by nitrogen adsorption-desorption isotherms obtained from BET analysis, as detailed in Section S2 (Figure S2), confirming the mesoporous nature of the samples.

The extent of Ca and Mn incorporation in the CLMN samples was evaluated using EDX and ICP-OES., with the results summarized in Table 3. Both techniques confirmed successful doping of Ca and Mn,

 Table 2

 Experimental conditions during material activation and CL-RWGS processes.

Parameter	Oxidation	Reduction *	RWGS
Temperature (°C) H2/CO2 molar ratio	600 – 900	600 – 900	600 – 900 0.75 – 1.3
Volumetric feed gas composition	$O_2 = 10$	$H_2 = 20$	$H_2 = 20; 17.5;$
(vol%)	$N_2 = 40$ He = 50	He = 10 $N_2 = 70$	15 $CO_2 = 15; 17.5;$
			20 He = 65
Feed flow rate (sccm)	400	400	400

Reduction refers to experimental conditions used during material activation.

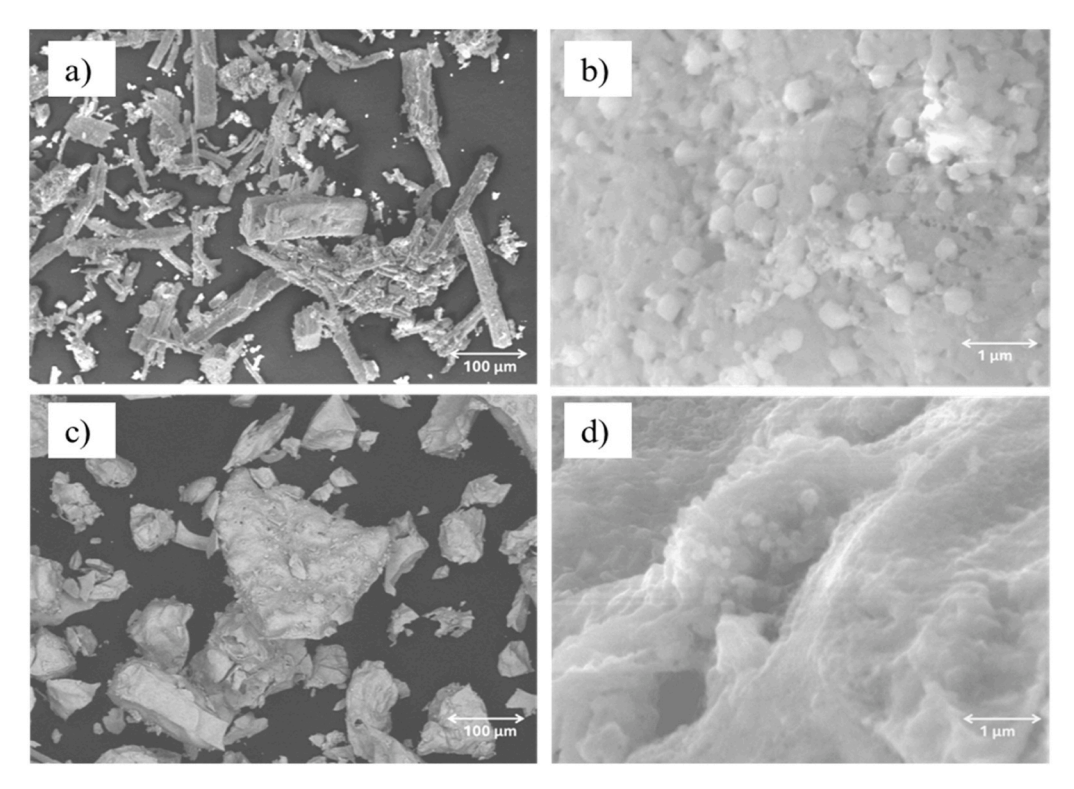


Fig. 2. SEM Images of a) Low magnified LaNiO3; b) High magnified LaNiO3; c) Low magnified CLMN-2 sample and d) High magnified CLMN-2 sample.

Table 3 ICP and EDX analysis of Ca and Mn content in CLMN samples.

Sample ID	Ca (wt%)		Mn (wt%)	
	ICP	EDX	ICP	EDX
CLMN-1	7 %	7 %	11 %	12 %
CLMN-2	8 %	7 %	11.5 %	13 %
CLMN-3	9 %	8 %	12 %	14 %

with concentrations increasing in the order CLMN-1 < CLMN-2 < CLMN-3. Moreover, the differences in measured wt% values between ICP-OES and EDX analyses were minimal (ca. ≤ 2 %), indicating good agreement between the methods and consistent dopant distribution across the samples.

Fig. 3 (a-d) presents the TEM micrographs of the LaNiO $_3$ and CLMN samples, highlighting changes in particle morphology and size distribution. A distinct shift in particle size distribution was observed with increasing Ca dopant concentration. While LaNiO $_3$, CLMN-1 and CLMN-2 exhibit hollow-like structures, CLMN-3, which contains the highest Ca content, shows pronounced signs of sintering and particle agglomeration, which also consistent with reduced SSA observed in BET measurements. As shown in Table 4, the SSA increased from 8.4 m²/g for LaNiO $_3$ to 9.8 m²/g and 12.1 m²/g for CLMN-1 and CLMN-2, respectively. However, a further increase in Ca content led to a decrease in SSA to 10.7 m²/g for CLMN-3. This behaviour aligns with the findings of Yang et al. [41], who also observed increased particle agglomeration in La-based material when Ca loading exceeded 10 wt%.

3.1.2. Powder X-ray diffraction (XRD) analysis

A comparison of XRD diffractograms of LaNiO $_3$ and all CLMN samples is presented in Fig. 4. The XRD pattern of LaNiO $_3$ exhibits characteristic diffraction peaks at $2\theta=23.0^\circ$ (101), 32.5° (110), 47.3° (202) and 58.5° (104), consistent with JCPDS File no. 330711 [42]. Additionally, diffraction peaks at 37.5° and 43.3° , corresponding to the (111) and (200) planes of NiO, respectively, indicate the presence of B-site NiO phases on the surface of LaNiO $_3$. The XRD patterns of all CLMN samples

closely resemble that of $LaNiO_3$, suggesting that no major secondary phases were formed. However, a reduction in the intensity of NiO-related peaks was observed in all CLMN samples, particularly at the prominent reflections corresponding to the (110), (201), and (101) planes. This reduction implies a decreased fraction of segregated NiO in the doped materials.

The inset of Fig. 4 shows a shift of the (110) diffraction peak toward lower 2θ values, attributed to the substitution of Ca and Mn for La and Ni in the A and B sites, respectively, within the perovskite lattice [43,44]. Ca^{2+} (1.00 Å) has a smaller ionic radius than La^{3+} (1.032 Å), while Mn^{3+} (0.645 Å) is larger than Ni^{3+} (0.56 Å). These substitutions lead to an overall expansion of crystal lattice (increased d-spacing), resulting in the peak shift toward lower diffraction angles according to Bragg's law [45]. Moreover, weak diffraction peaks corresponding to CaO and Mn₂O₃ phases were detected at higher 2θ values, likely due to the relatively low dopant concentrations. A weak shoulder near the (110) peak was observed in samples with lower Ca and Mn contents, indicating incomplete incorporation of Mn into the Ni-containing lattice. This suggests the presence of minor secondary phases and localized lattice distortions [46]. In contrast, more uniform incorporation of Mn³⁺ was observed in the CLMN-3 sample, as confirmed by EDX mapping (Figure S3a-f), which coincided with the disappearance of the shoulder peak.

The primary crystallite size of $LaNiO_3$ and all CLMN samples was estimated using the Debye-Scherrer equation, as described in Section S4 (Table S1). An increase in crystalline size was observed with higher dopant concentrations, specifically, the crystallite size of CLMN-3 was 15 nm, compared to 10 nm for $LaNiO_3$, suggesting structural modifications and lattice expansion due to Ca and Mn incorporation. Furthermore, the Goldschmidt tolerance factor (GTF) for $LaNiO_3$ and all CLMN samples ranged from 0.93 to 0.94 (Table S1), indicating the formation of stable perovskite structures. The detailed methodology for calculating GTF values is provided in Section S4.

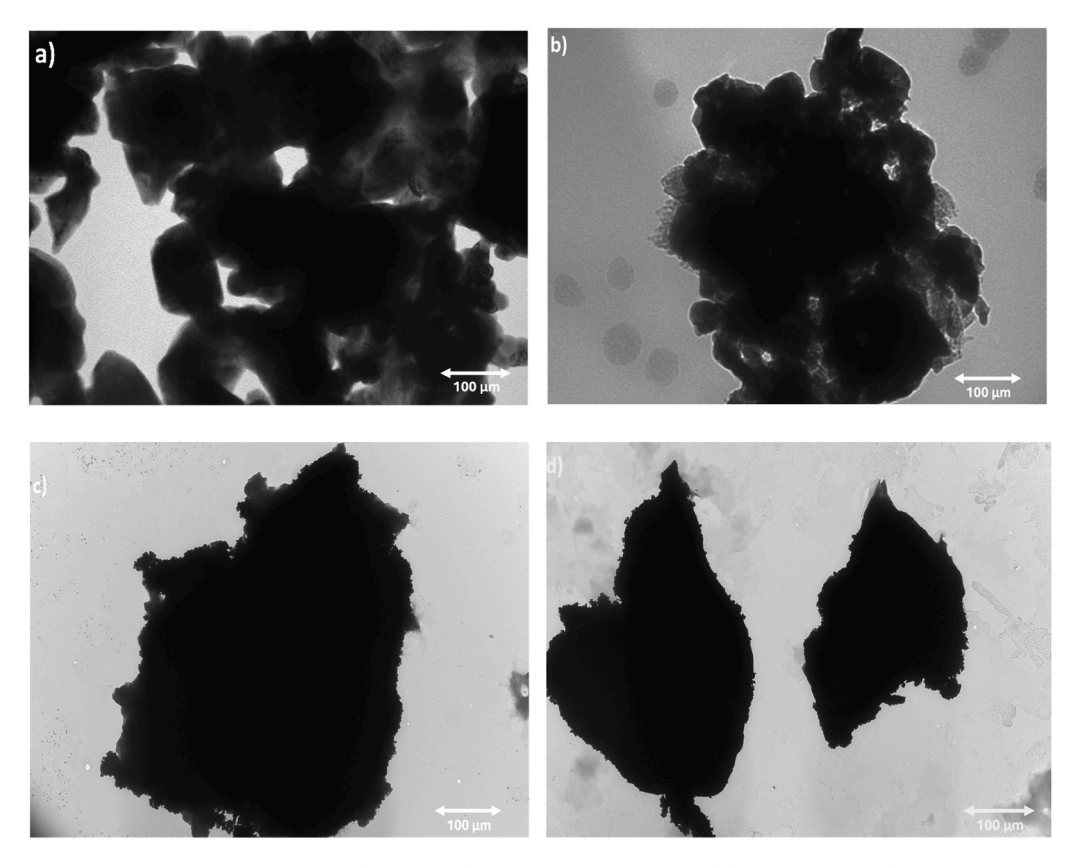


Fig. 3. TEM images of a) LaNiO₃; b) CLMN-1; c) CLMN -2 and d) CLMN -3 samples.

Table 4 Specific surface area (SSA, $\rm m^2/g)$ and pore volume (cm $^3/\rm g)$ of LaNiO $_3$ and CLMN samples.

Sample	Surface area (m ² /g)	Specific pore volume (cm ³ /g)
LaNiO ₃	8.4	0.012
CLMN-1	9.8	0.012
CLMN-2	12.1	0.017
CLMN-3	10.7	0.014

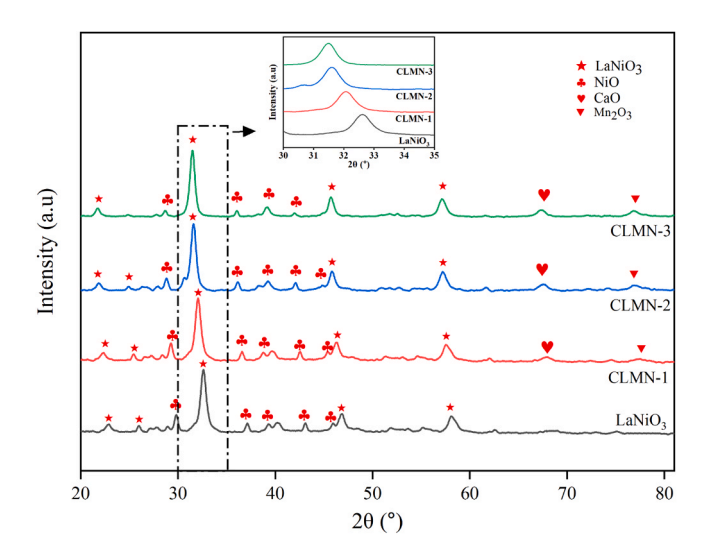


Fig. 4. Powder X-ray diffractograms of $LaNiO_3$ and CLMN samples (Inset graph shows a shift in diffraction peak at 110 plane).

3.2. Stability and oxygen storage capacity

As shown in Fig. 5a, all CLMN samples underwent 17 consecutive high-temperature redox cycles, exhibiting minimal degradation (<0.5 %) across the 700 – 900 °C range. This indicates strong structural stability and suggests that CLMN materials are well-suited for OSR applications [47–49]. The oxygen storage capacity (mmol O_2/g_{OSR}) of all CLMN samples during successive redox cycles was calculated (Eq. 1) at 900, 850, 800, 750 and 700 °C, and results are reported in Fig. 5b. Among all the samples, CLMN-2 exhibited the highest oxygen storage capacity during H_2 reduction, reaching 1.97 mmol O_2/g_{OSR} (6.32 wt%). An initial \sim 10 % decrease in oxygen storage capacity during the first cycle at 900 °C was attributed to material activation during the initial two cycles. Subsequently, only a slight reduction in oxygen storage capacity was observed for all CLMN samples over multiple cycles at various temperatures, indicating good redox stability and recyclability.

At higher temperatures, all CLMN samples showed increased oxygen storage capacity, likely due to thermal expansion enhancing atomic interaction between A-site and B-site cations in the perovskite lattice, thereby promoting release of lattice oxygen [50]. Additionally, the increased porosity of Ni layers at elevated temperatures facilitated the formation of porous NiO circular caps, improving contact between the fuel gas and the B-site cations, which in turn enhanced lattice oxygen transfer and overall oxygen storage capacity [51]. Notably, CLMN-2 consistently demonstrated higher oxygen storage capacity values than CLMN-1 and CLMN-3 across all temperatures, likely due to its relatively greater SSA and pore volume. The oxygen storage capacity of CLMN-2 was also compared with LaNiO3 over the 700 - 900 °C range to examine any trade-off due to Ca doping. Figure S4 shows that LaNiO₃ exhibited lower oxygen storage capacity than CLMN-2 at 800-900 °C, while both samples showed similar values at 700 and 750 $^{\circ}$ C. These findings underscore the promising redox characteristics of CLMN-2, justifying its selection for subsequent evaluation in a packed bed

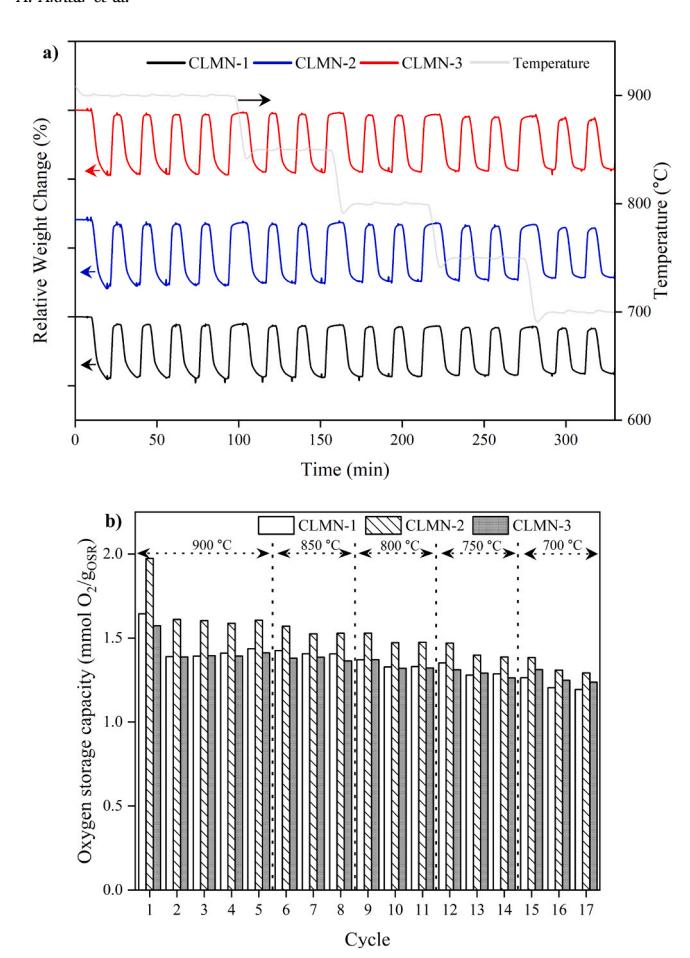


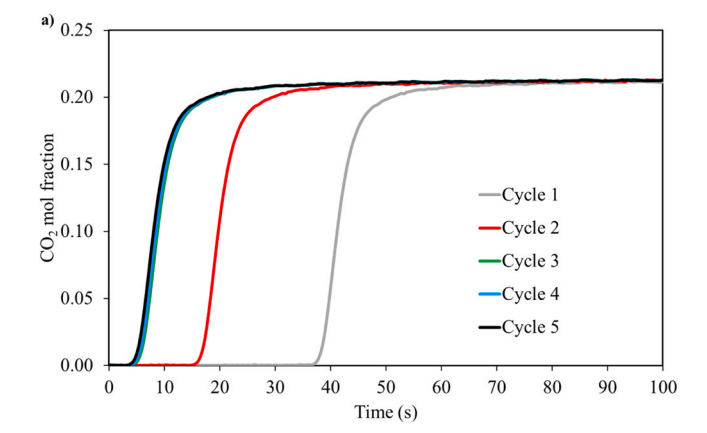
Fig. 5. TGA performance of each CLMN sample for various temperatures; $H_2 = 3.6$ vol%, $O_2 = 16$ vol%. **a)** cyclic stability and **b)** Oxygen storage capacity comparison for all CLMN samples in the 700 - 900 °C range.

reactor setup.

3.3. Sorption and CL-RWGS experiments

3.3.1. Carbonation/calcination cycles

To evaluate the CO₂ sorption performance of CLMN-2, five consecutive carbonation-calcination cycles were conducted in a packed bed reactor loaded with 1.0 g of the CLMN-2 sample. The CO₂ breakthrough curves for the initial five cycles are presented in Fig. 6a, with the first cycle showing a distinct breakthrough time of ~40 s. Based on the carbon material balance, it was observed that CLMN-2 achieved a CO₂ uptake of 2.4 mmolCO₂/g_{OSR} during first cycle, yielding a 46 % of CO₂ sorption efficiency. Fig. 6b shows the CO₂ sorption efficiency of CLMN-2 over all five cycles. A notable 28 % reduction in sorption efficiency was observed between the first two cycles, indicating a diminished ability of CLMN-2 for CO₂ uptake and, consequently, a lower conversion of CaO to CaCO₃. The CO₂ sorption efficiency further dropped to 6 % in the third cycle and remained consistent thereafter. This decline in sorption performance during initial cycles is likely due to sintering, which may have resulted from the growth of CaO particles and the formation of microphases from metal oxides other than CaO [52]. The associated increase in primary crystal size reduces the reactive surface area, thereby limiting both the rate and extent of gas-solid carbonation reactions [53, 54]. A similar decreasing trend in CaO conversion during CaL operation was reported by Abbas et al. [55], where CO2 sorption efficiency decreased from 40 % in the first cycle to below 10 % by the fourth cycle. Moreover, other studies have also reported a sharp decline in CO₂ sorption capacity using CaO, emphasizing the need of adding structural



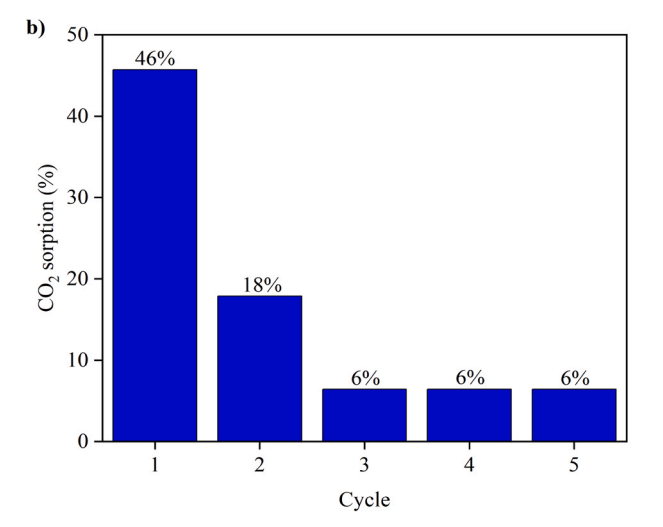


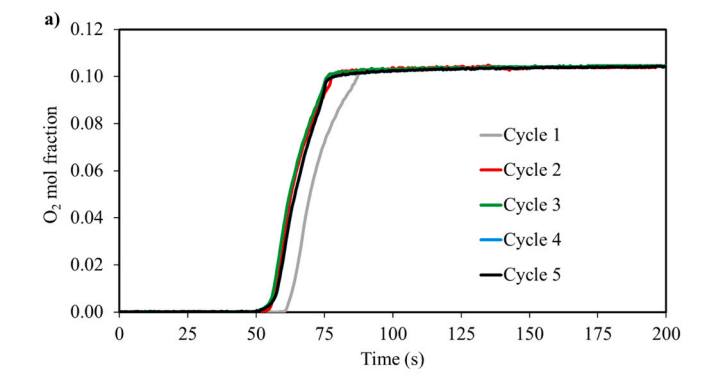
Fig. 6. a) $\rm CO_2$ breakthrough curves during carbonation cycles and b) $\rm CO_2$ sorption efficiency (%) of CLMN-2 at 600 °C, 1.0 bar, a total feed flow rate of 400 sccm with 20 vol% $\rm CO_2$ (He and $\rm N_2$ to balance).

promoters [56,57].

3.3.2. Material activation

A series of consecutive redox cycles were initially conducted to activate the CLMN-2 sample. The activation process was carried out in the same packed bed reactor used for subsequent evaluations. Redox cycling was extended beyond the breakthrough point and continued until a steady-state conversion profile was achieved, ensuring that the material exhibited stable redox behaviour under cyclic operations. As shown in Fig. 7a, the O₂ breakthrough profiles across five consecutive oxidation cycles at 800 °C and 1 bar (10 vol% O₂ in N₂) were reproducible. The O₂ uptake duration was \sim 1 min per cycle, indicating that the material had reached a stable operating state. No significant variation was observed in the outlet gas composition after the first cycle, confirming successful activation of the material. Furthermore, the H₂ breakthrough time during the reduction step was similar to the O₂ breakthrough time during oxidation, as stoichiometric feed gases with a molar O₂:H₂ ratio of 0.5 were used.

To evaluate the influence of temperature on the reduction performance of CLMN-2, the reduction step was carried out over the temperature range of $600-900\,^{\circ}$ C, while oxidation was consistently performed at $800\,^{\circ}$ C. As shown in Fig. 7b, the highest oxygen uptake was achieved at $900\,^{\circ}$ C. This enhancement is attributed to the thermal expansion and oxygen release associated with the B-site of perovskite material, which increases porosity and oxygen vacancies, thereby facilitating bulk oxygen diffusion [58]. Additionally, the oxygen storage capacity measured in the packed bed reactor showed a maximum $2.1\,\mathrm{mmol}\,O_2/g_{OSR}$ at $900\,^{\circ}$



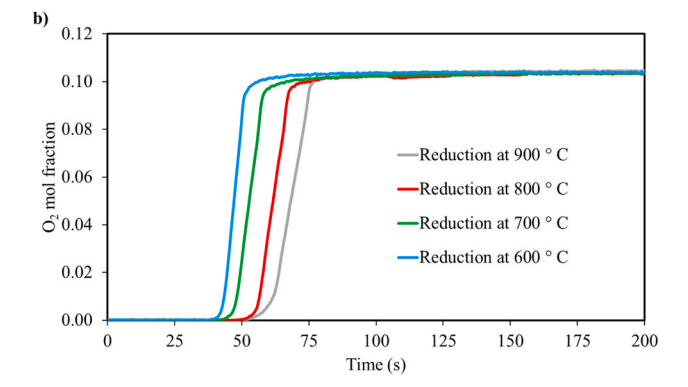


Fig. 7. a) Evolution of O_2 breakthrough curves during oxidation for CLMN-2 at 800 °C, 1.0 bar, total feed flow rate of 400 sccm and 10 vol% O_2 in feed over 5 cycles; **b)** O_2 breakthrough curves with reduction temperature varying across 600 – 900 °C (Oxidation temperature = 800 °C, 1.0 bar, total 400 sccm feed flow rate, 0.5 O_2/H_2 molar ratio during redox cycles).

 $^{\circ}$ C, consistent with the TGA results (Fig. 5). The slightly higher oxygen storage capacity observed in the reactor compared to TGA can be attributed to differences in H₂ concentration. 20 H₂ was used in the reactor under RWGS representative conditions, compared to 4 H₂ in the TGA setup due to safety constraints.

3.3.3. Reverse water-gas shift (RWGS) reaction experiments

Following the activation of CLMN-2, the RWGS reaction was carried out under a range of operational parameters, outlined in Table 2. Fig. 8a presents the molar composition of the outlet gas (dry basis) consisting of unreacted CO $_2$, CO and H $_2$ during the RWGS step, performed at atmospheric pressure and 900 °C with a feed gas comprising H $_2$ /CO $_2$ molar ratio of 1.3. The product gas composition was recorded after reaching steady state, yielding H $_2$ /CO molar ratio of 1.25. Notably, no CH $_4$ was detected during the CL-RWGS process, indicating the absence of CO $_2$ methanation. This observation is consistent with the thermodynamic understanding that the Sabatier reaction is favoured at temperatures \leq 300 °C [59], which is well below the 600 – 900 °C range employed in this study.

To elucidate the effects of temperature and feed gas composition on the $\rm H_2/CO$ product molar ratio, RWGS experiments were conducted over a range of $\rm H_2/CO_2$ molar ratio (0.75 – 1.3) and temperatures (600 – 900 °C). As shown in Fig. 8b, at a fixed $\rm H_2/CO_2$ molar ratio of 1.3, increasing the reaction temperature from 600 to 900 °C decreased the $\rm H_2/CO$ product molar ratio from 2.40 to 1.25. This trend is consistent with the endothermic nature of the RWGS reaction, where higher temperatures enhance CO generation by consuming more $\rm H_2$, thereby lowering the $\rm H_2/CO$ molar ratio [60].

Besides temperature, the feed $\rm H_2/CO_2$ molar ratio has a direct effect on the product composition. At 600 °C, increasing the feed $\rm H_2/CO_2$ molar ratio from 0.75 to 1.3 increased the $\rm H_2/CO$ molar ratio from 1.58 to 2.40. This occurs because a lower $\rm CO_2$ concentration in the feed limits

CO formation, resulting in excess unreacted H_2 and thus a higher H_2 /CO ratio in the product gas. Based on these results, 1.0 feed molar ratio of H_2 /CO₂ at 600 °C produced H_2 /CO product molar ratio of \sim 2.0, which is favourable for FTS [61]. Additionally, the CO/CO₂ yield ratio was evaluated over the same range of feed compositions and temperatures, as illustrated in Fig. 8c. The data indicate that the highest CO yield was achieved at 900 °C. Error bars in Fig. 8b,c represents the standard deviation from at least three independent measurements.

The experimentally obtained H2/CO molar ratios and CO2 conversion efficiencies over the temperature range of 600 – 900 °C and H₂/CO₂ molar feed ratios of 0.75 - 1.3 were compared with the equilibrium values calculated using RGibbs reactor simulations performed in Aspen PLUS® V14. The simulation conditions were aligned with the experimental set-up conditions described in Table 2. It was observed that although the H₂/CO molar ratio did not reach equilibrium values throughout the experiments, the deviation from the equilibrium was negligible at 900 °C. Notably, H2/CO molar ratios approaching the target value of ~2.0, considered optimal for FTS, were achieved at lower temperatures, specifically at 600 °C and 700 °C for H2/CO2 feed molar ratios of 1.0 and 1.3, respectively, as shown in Fig. 9a. The CO₂ to CO conversion efficiency of CLMN-2 was evaluated. As shown in Fig. 9b, a CO₂ conversion of 57.4 % was obtained during RWGS operation at 900 C, closely matching the equilibrium conversion of 60 % under the same conditions (H₂/CO₂ molar ratio of 1.3). The CO₂ conversion of 57.4 % achieved in this work surpasses the values reported in previous co-fed CL-RWGS studies [62,63], thereby underscoring the promising potential of CLMN-2. Even at 600 $^{\circ}$ C and H₂/CO₂ molar ratio of 1.0, \sim 86 % of the predicted CO₂ conversion was achieved, with a corresponding molar ratio of H₂/CO ~2.0. The presence of unconverted CO₂ suggests the potential for integration of CO2 capture upstream of the FTS step, allowing its reuse within the CL-RWGS system [28]. Overall, these findings highlight the favourable performance of CLMN-2 in the CL-RWGS process, demonstrating its potential as a competitive material for syngas production compared to conventional technologies.

3.3.4. Complete cycle of CL-RWGS

To evaluate the performance of CLMN-2 in the CL-RWGS process, 1.0 g of CLMN-2 was loaded into the packed bed reactor. Prior to the CL-RWGS experiments, CLMN-2 was subjected to five successive redox cycles at 600 °C under the operating conditions listed in Table 2 to ensure reproducible performance. Between each cycle, He (200 sccm) was used as a purge gas for \sim 120 s to remove residual gases in the lines.

Fig. 10 shows a complete cycle of CL-RWGS process using activated CLMN-2. A mixture of CO₂ and H₂ (He gas to balance) with a molar ratio of 1.3 was introduced into the reactor simultaneously, and this point was designated as t = 0 for data acquisition. As shown in Fig. 10, neither CO_2 nor H₂ was detected at the reactor outlet during the initial ~90 s of the complete cycle, indicating that CLMN-2 simultaneously facilitated CO2 absorption and reduction. H2 material balance showed that 7.22 mmol/ g_{OSR} of H₂ was consumed during the initial reduction. Moreover, no CO breakthrough curve was observed during this period, suggesting that the RWGS reaction did not occur during the first ~120 s of the cycle. After this time, the RWGS reaction was initiated, as syngas (CO and H₂) was generated with H₂/CO molar ratio of 2.4, and 3.74 mmol/g_{OSR} of H₂ was consumed during the RWGS stage. This indicates that CaO predominantly facilitated the initial CO2 sorption, whereas oxygen vacancies within the perovskite lattice contributed to the CO₂ conversion during the RWGS stage, leading to CO formation. After reaching steady state reaction conditions, with CO2 to CO conversion reaching 35 % after ~240 s, feed gas was switched to only He for 120 s to remove residual product gases, preparing the system for the next cycle. Once the outlet gas composition confirmed the presence of He only, the oxidation phase was initiated by introducing 200 sccm of diluted air (10 O2) to fully regenerate CLMN-2 for subsequent CL-RWGS cycles. At this stage, N₂ and He were the primary gases detected at the reactor outlet. After 90 s of introducing air, O2 breakthrough was observed, and the outlet

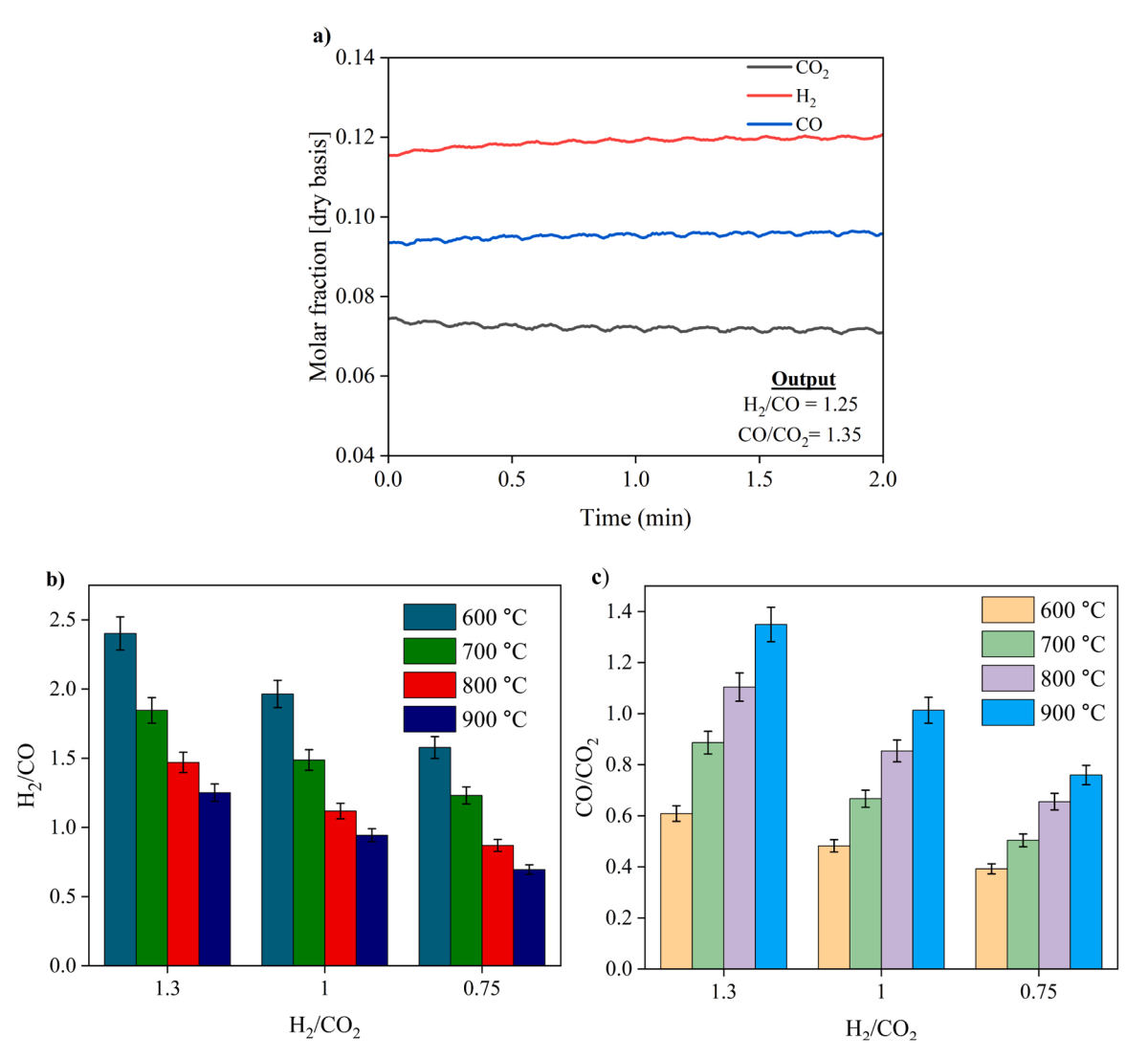


Fig. 8. a) Product molar composition at 900 °C, 1 bar and an H_2/CO_2 molar feed ratio of 1.3; b) H_2/CO molar ratio at various H_2/CO_2 molar ratios (0.75 – 1.3) and temperatures (600 – 900 °C); and c) CO/CO_2 molar ratio at different H_2/CO_2 molar ratio (0.75 – 1.3) and temperatures (600 – 900 °C).

composition stabilized after consuming 2.75 mmol/gosR of O_2 to regenerate CLMN-2. The air feed was then switched off, and He was used to purge the reactor for 120 s. Following this, the furnace temperature was increased to 900 °C to initiate the calcination step, aimed at desorbing CO_2 adsorbed by the material. As shown in Figure S5, CO_2 was detected during calcination, confirming that CO_2 had been adsorbed by the material in the earlier stage. A comprehensive breakdown of the reaction schemes involved and carbon balance in product gas during each step for complete cycle is presented in Table 5. All equations used for calculating carbon molar balance are also provided in section S7 of SI (Eqs. S3 – S9).

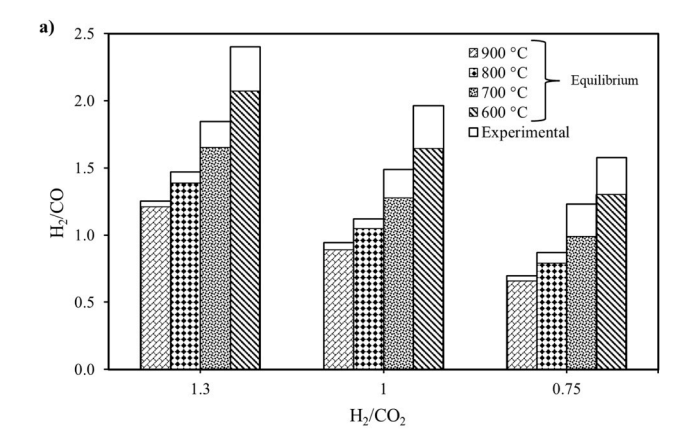
 CO_2 was also detected at the reactor outlet during air oxidation, suggesting carbon formation during the process, which was also observed during the CL-RWGS at 700 °C. The carbon deposition at 600 and 700 °C can be attributed to the reverse Boudouard reaction (2CO \rightarrow $CO_2 + C$), which is thermodynamically favoured at these temperatures. The resulting carbon undergoes combustion in the presence of air, releasing CO_2 [64]. However, no evidence of carbon deposition was observed at higher temperatures, likely due to the thermodynamics favouring CO formation during the reduction phase. In addition, the presence of Ni in the material is known to promote carbon formation [65]. For CLMN-2, a carbon balance revealed that up to 0.35 mmol CO_2/g_{OSR} was released during air oxidation stage, as shown in Table 5. According to the stoichiometry of the carbon oxidation reaction $(C + C_2)$

 \rightarrow CO₂), this CO₂ release corresponds to 0.35 mmol of deposited carbon. This indicates approximately 2.8 % of the total carbon fed was deposited through reverse Boudouard reaction, which aligns with the values reported in the literature [38,51]. The low carbon deposition underscores the role of Mn in reducing carbon formation via its multi-valent redox ability and improved oxygen storage capability [66].

These preliminary findings support the potential of CLMN-2 as a multifunctional material for the CL-RWGS process, demonstrating its ability to simultaneously facilitate reduction and $\rm CO_2$ sorption. Further research should focus on detailed investigation into the temperature distribution within the packed bed reactor to gain deeper insight into the system's thermal behaviour and practical performance.

3.4. Post experimental characterization

Following multiple CL-RWGS cycles, the CLMN-2 sample was subjected to post experimental characterization using XRD, SEM and BET analysis evaluate changes in the crystallite structure, phase and morphology compared to the fresh material. The XRD pattern of used CLMN-2 revealed no significant change in crystallite structure after over 12 h of CL operation (Figure S6). However, slight broadening of multiple peaks was observed, likely due to repeated redox cycling and exposure to high temperature calcination at 900 °C. Partial segregation of the CaO phase was also observed, which is thermodynamically favoured at high



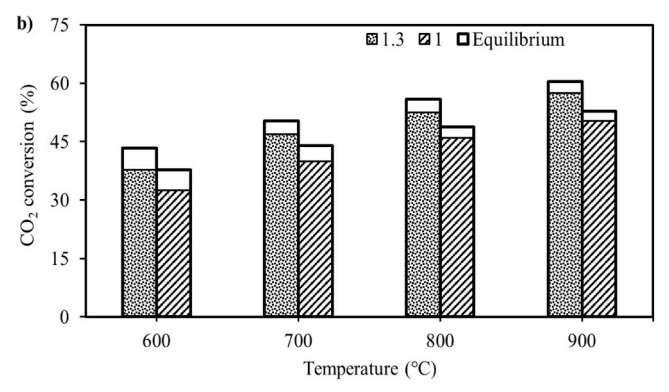


Fig. 9. Comparison between experimental and equilibrium values across the $600-900\,^{\circ}\text{C}$ range for **a)** H_2/CO molar ratio (molar feed gas ratio 0.75-1.3) and **b)** CO_2 conversion (%) at H_2/CO_2 molar ratio of 1.0 and 1.3.

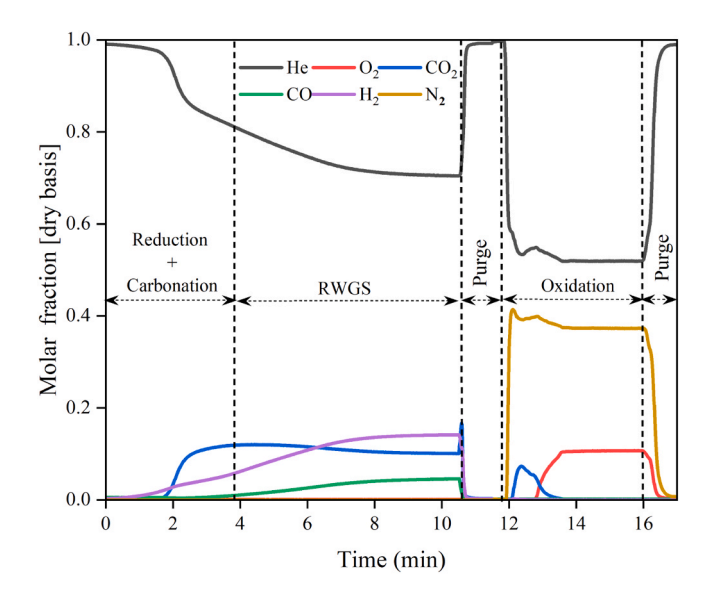


Fig. 10. Complete cycle of CL-RWGS process with simultaneous CO_2 capture through carbonation at 600 °C, 1.0 bar and H_2/CO_2 feed molar ratio of 1.3.

temperatures [67]. In addition, Williamson-Hall analysis (Figure S7) on XRD data was performed to quantify the change in the lattice strain between fresh and used CLMN-2 samples, as described in **Section S8** (SI file). The lattice strain increased from 0.0085 in the fresh sample to 0.0163 in the used sample as shown in Table S2 (SI file), representing an approximate 92 % increase. This strain growth indicates the development of microcracking, causing internal stress within the crystal lattice [68,69]. Hence, a decline in CO₂ sorption efficiency during initial cycles

Table 5Main reactions and carbon molar balance during complete cycle of CL-RWGS process with in-situ carbonation involving CLMN-2.

Process	Reaction	Carbon material balance in product gas (mmol)
Carbonation	CO_2 + $^{\ddagger}CaO \rightarrow CaCO_3$	_
Reduction	$\delta H_2 + Ca_{0.2}La_{0.8}Mn_{0.1}Ni_{0.9}O_3 \rightarrow$	-
	$Ca_{0.2}La_{0.8}Mn_{0.1}Ni_{0.9}O_{3\cdot\delta} + \delta H_2O$	
CO ₂ splitting	$Ca_{0.2}La_{0.8}Mn_{0.1}Ni_{0.9}O_{3-\delta} + (\delta-*\gamma) CO_2$	7.05 (excess CO ₂)
	\rightarrow Ca _{0.2} La _{0.8} Mn _{0.1} Ni _{0.9} O _{3-γ} + (δ - γ) CO	4.26 (CO)
Air Oxidation	$Ca_{0.2}La_{0.8}Mn_{0.1}Ni_{0.9}O_{3-\gamma} + \frac{\gamma}{2}O_2 \rightarrow$	-
	Ca _{0.2} La _{0.8} Mn _{0.1} Ni _{0.9} O ₃	
Combustion of deposited carbon	$C + O_2 \rightarrow CO_2$	0.35
Calcination	$CaCO_3 \rightarrow CaO + CO_2$	0.65

[‡]CaO refers to the CaO phase in CLMN-2.

is observed as shown in Fig. 6b [70]. In addition, no new secondary NiO phases were detected within the 2θ range of $37.8\text{-}45.1^\circ$, confirming that the bulk perovskite structure remained largely intact without any nickel formation. Morphological analysis further supported these findings. As shown in Fig. 11a-b, the used CLMN-2 sample retained its overall particle size and shape after experimentation, with no significant surface degradation or structural deformation observed. However, a noticeable change in surface roughness was apparent, suggesting decrease in porosity was further corroborated by post experimental BET analysis. As shown in Table S2, the SSA of CLMN-2 decreased from $12.1~\text{m}^2/\text{g}$ to $0.44~\text{m}^2/\text{g}$ after the experimental run. This substantial change in SSA is attributed to the sintering of CaO phase within CLMN-2 during successive CaL cycles [57].

3.5. Environmental implications and future work

Compared to the conventional RWGS process, the CL-RWGS with CLMN-2 material yields a more favourable molar ratio of H2/CO that aligns with the requirements of FTS. While comparing the experimental molar ratio of H₂/CO with the conventional equilibrium values (Fig. 9a), CL-RWGS achieved H_2/CO molar ratio of ~ 2.0 at a molar feed ratio (H_2/CO) CO₂) of 1.0, whereas the conventional equilibrium RWGS process requires a molar feed ratio (H₂/CO₂) of 1.3 to reach a similar syngas composition. This indicates that the CL-RWGS using CLMN-2 produces favourable syngas compositions (H2/CO ~2.0) while consuming 23 % less H2. Given that producing H2 from water electrolysis and steam methane reforming processes are energy-intensive [71–73], its lower consumption in CL-RWGS by using CLMN-2 suggests reduction in energy penalties as compared to conventional RWGS process. Thus, utilizing CLMN-2 in CL-RWGS presents a promising reaction pathway to reduce CO₂ emissions from heavy industries such as steel and iron production. This process specifically targets CO2-rich flue gases emitted by heavy industries, which are significant contributors to global greenhouse gas emissions. Incorporating in-situ CO2 sorption further enhances the redox performance of CLMN-2 during CL-RWGS. Since carbonation is exothermic, the heat released can be integrated in the endothermic initial reduction step, thereby increasing the reduction breakthrough time and the oxygen storage capacity of CLMN-2. The high performance of CLMN-2 in achieving an optimal H2/CO molar ratio of 2.0 makes it particularly advantageous for downstream FTS process, facilitating the production of synthetic fuels. Furthermore, using CLMN-2 in ICCU applications can reduce energy intensity compared to conventional technologies that capture and convert CO₂ in separate steps. Therefore, the approach presented in this study supports broader efforts to adopt low-carbon technologies and meet net-zero emission targets. Future research will focus on a comprehensive evaluation of CLMN based

^{*} γ denotes partial oxygen storage (0 < γ < δ).

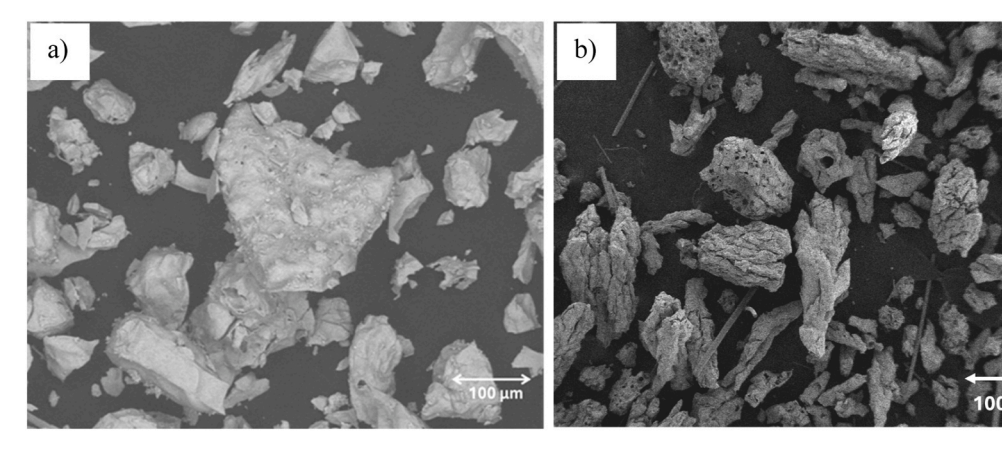


Fig. 11. SEM images of a) fresh CLMN -2 and b) aged CLMN-2 samples.

performance by simulating real flue gas composition to bridge the gap between lab-scale results and practical retrofitting in energy-intensive industries. Moreover, the calcination temperature will also be optimized, particularly for large scale use of CLMN-2, since the heat released during air oxidation can facilitate $\rm CO_2$ desorption without the need for excessive external heating.

Furthermore, equilibrium limitations can be surpassed through counter-current operations, as demonstrated in studies reporting CO_2 conversions of up to 90 % [74,75]. This enhancement can be attributed to consistent heat gradient throughout the reactor during interaction between feed gases and OSR material [76]. Therefore, the performance of CLMN based material in a counter current CL-RWGS setup will be examined to further improve CO_2 conversion efficiency.

4. Conclusions

A novel Ca/Mn-doped LaNiO₃ perovskite was synthesized and evaluated as multifunctional material with integrated oxygen storage and release (OSR) and dual functional material (DFM) capabilities for ICCU applications. Among the synthesized variants, Ca_{0.2}La_{0.8}Mn_{0.1}Ni_{0.9}O₃ (CLMN-2) exhibited highest performance, achieving an oxygen storage capacity of 6.2 wt% (1.97 mmol O₂/g_{OSR}) with negligible degradation over 17 consecutive cycles. These results provided a basis for evaluating the material under realistic conditions in a packed bed reactor. CLMN-2 demonstrated consistent redox behaviour and effective CO2 sorption at 600 °C. Under CL-RWGS conditions, it achieved a maximum CO2 to CO conversion of 57.4 % was achieved at 900 $^{\circ}$ C and H₂/CO₂ molar feed gas ratio of 1.3, which corresponds to 95 % of equilibrium conversion. At 600 °C and H₂/CO₂ molar ratio 1.0, a produced syngas stream with H₂/ CO molar ratio of 2.0 was obtained. These findings confirm the material's combined DFM and OSR functionalities and underscore its potential for scalable syngas production. Future work will focus more on extensive testing by integrating a range of feed gas composition and residence time. In addition, the heat distribution within the reactor will also be monitored to understand the effect of temperature fluctuations on material's activity, stability, and overall efficiency of the CL-RWGS process.

CRediT authorship contribution statement

Adam Zaidi: Writing – review & editing, Methodology, Formal analysis, Data curation. Christopher de Leeuwe: Writing – review & editing, Data curation, Conceptualization. Angelos M. Efstathiou: Writing – review & editing, Visualization. Anam Asghar: Writing – review & editing, Investigation. Hassan-Sayed Mohamed: Writing – review & editing, Validation, Supervision. Syed Zaheer Abbas: Writing – review & editing, Validation, Supervision, Resources, Project administration, Funding acquisition, Conceptualization. Adnan Akhtar:

Writing – original draft, Visualization, Validation, Software, Methodology, Investigation, Formal analysis, Data curation, Conceptualization.

Declaration of Competing Interest

The authors declare that they have no known competing financial interests or personal relationships that could have appeared to influence the work reported in this paper.

Acknowledgements

The authors would like to thank the School of Chemistry and Chemical Engineering, University of Southampton for providing necessary research funding for this study. Moreover, the authors would also like to acknowledge Dr. Vincenzo Spallina for providing access to the laboratory at the University of Manchester in the Sustainable PRocess INtensification Group (SPRING).

Appendix A. Supporting information

Supplementary data associated with this article can be found in the online version at doi:10.1016/j.jece.2025.119640.

Data availability

Data will be made available on request.

References

- [1] IEA (International Energy Agency), Global Energy Review: CO2 Emissions in 2021, IEA, Paris (2021). (https://iea.blob.core.windows.net/assets/c3086240-732b-4f6a-89d7-db01be018f5e/GlobalEnergyReviewCO2Emissionsin2021.pdf) (accessed March 3, 2025).
- [2] H. bo Wu, M. xin Xu, Y. bing Li, J. hua Wu, J. chong Shen, H. Liao, Experimental research on the process of compression and purification of CO2 in oxy-fuel combustion, Appl. Energy 259 (2020) 114123, https://doi.org/10.1016/J. APENERGY.2019.114123.
- [3] B. Jin, K. Wei, T. Ouyang, Y. Fan, H. Zhao, H. Zhang, Z. Liang, Chemical looping CO2 capture and in-situ conversion: fundamentals, process configurations, bifunctional materials, and reaction mechanisms, Appl. Energy Combust. Sci. 16 (2023) 100218. https://doi.org/10.1016/J.JAECS.2023.100218.
- [4] Y. Zhang, S. Zhao, L. Li, J. Feng, K. Li, Z. Huang, H. Lin, Integrated CO 2 capture and utilization: a review of the synergistic effects of dual function materials, Catal. Sci. Technol. (2024).
- [5] L. Chen, D. Liu, G. Wei, Performance of Na-Ru/Al2O3 dual function material for integrated CO2 capture and methanation with the presence of coal ashes, Energy Convers. Manag 299 (2024) 117811, https://doi.org/10.1016/J. ENCONMAN 2023 117811
- [6] R. Han, Y. Wang, L. Wei, M. Peng, Z. Li, C. Liu, Q. Liu, Integrated CO2 capture and conversion by Cu/CaO dual function materials: effect of in-situ conversion on the sintering of CaO and its CO2 capture performance, Carbon Capture Sci. Technol. 12 (2024) 100220, https://doi.org/10.1016/J.CCST.2024.100220.

- [7] C. Molinet-Chinaglia, S. Shafiq, P. Serp, Low temperature sabatier CO2 methanation, ChemCatChem 16 (2024) e202401213, https://doi.org/10.1002/ cete.202401213
- [8] B. Agún, A. Abánades, Comprehensive review on dry reforming of methane: challenges and potential for greenhouse gas mitigation, Int J. Hydrog. Energy 103 (2025) 395–414, https://doi.org/10.1016/J.IJHYDENE.2025.01.160.
- [9] J. Liang, J. Liu, L. Guo, W. Wang, C. Wang, W. Gao, X. Guo, Y. He, G. Yang, S. Yasuda, B. Liang, N. Tsubaki, CO2 hydrogenation over Fe-Co bimetallic catalysts with tunable selectivity through a graphene fencing approach, Nat. Commun. 15 (2024) 512, https://doi.org/10.1038/s41467-024-44763-9.
- [10] M. Díaz, M. Alonso, G. Grasa, J.R. Fernández, The Ca-Cu looping process using natural CO2 sorbents in a packed bed: operation strategies to accommodate activity decay, Chem. Eng. Sci. 273 (2023) 118659, https://doi.org/10.1016/J. CES.2023.118659.
- [11] Y. Zhao, B. Jin, Z. Liang, Synergistic enhanced Ca–Fe chemical looping reforming process for integrated CO2 capture and conversion, Ind. Eng. Chem. Res 59 (2019) 1298–1307
- [12] Z. Sun, D.Y. Lu, R.T. Symonds, R.W. Hughes, Chemical looping reforming of CH4 in the presence of CO2 using ilmenite ore and NiO-modified ilmenite ore oxygen carriers, Chem. Eng. J. 401 (2020) 123481, https://doi.org/10.1016/J. CFJ 2019 123481
- [13] L. Zhang, L. Mei, K. Wang, Y. Lv, S. Zhang, Y. Lian, X. Liu, Z. Ma, G. Xiao, Q. Liu, Advances in the application of perovskite materials, Nanomicro Lett. 15 (2023)
- [14] H. Zhu, S. Teale, M.N. Lintangpradipto, S. Mahesh, B. Chen, M.D. McGehee, E. H. Sargent, O.M. Bakr, Long-term operating stability in perovskite photovoltaics, Nat. Rev. Mater. 8 (2023) 569–586.
- [15] A.S.R. Bati, Y.L. Zhong, P.L. Burn, M.K. Nazeeruddin, P.E. Shaw, M. Batmunkh, Next-generation applications for integrated perovskite solar cells, Commun. Mater. 4 (2023) 2, https://doi.org/10.1038/s43246-022-00325-4.
- [16] X. Yin, R. Zhang, Y. Zhang, S. Wang, L. Shen, Enhanced reactivity of methane partial oxidation of nickel doped LaMnO3+δ perovskites for chemical looping process, Int J. Hydrog. Energy 71 (2024) 481–492, https://doi.org/10.1016/J. LIHYDENE 2024 05 247
- [17] T. Dawa, B. Sajjadi, Exploring the potential of perovskite structures for chemical looping technology: a state-of-the-art review, Fuel Process. Technol. 253 (2024) 108022, https://doi.org/10.1016/J.FUPROC.2023.108022.
- [18] F. Wang, S. Chen, S. Chen, J. Du, L. Duan, W. Xiang, Double adjustment of ni and co in CeO2/La2Ni2-xCoxO6 double perovskite type oxygen carriers for chemical looping steam methane reforming, Chem. Eng. J. 465 (2023) 143041.
- [19] Y. Kim, H.S. Kim, D. Kang, M. Kim, J.W. Lee, Enhanced redox performance of LaFeO3 perovskite through in-situ exsolution of iridium nanoparticles for chemical looping steam methane reforming, Chem. Eng. J. 468 (2023) 143662, https://doi. org/10.1016/J.CEJ.2023.143662.
- [20] M. Barreau, D. Salusso, J. Zhang, M. Haevecker, D. Teschner, A. Efimenko, F. Bournel, J.-J. Gallet, E. Borfecchia, K. Sobczak, C. Petit, S. Zafeiratos, Uncovering the critical function of lanthanum in CH4 production from CO2 using exsolved LaNiO3 perovskite catalysts, J. Mater. Chem. A Mater. 12 (2024) 7605–7621, https://doi.org/10.1039/D3TA07391B.
- [21] J.A. Onrubia-Calvo, B. Pereda-Ayo, J.A. González-Marcos, J.R. González-Velasco, Lanthanum partial substitution by basic cations in LaNiO3/CeO2 precursors to raise DFM performance for integrated CO2 capture and methanation, J. CO2 Util. 81 (2024) 102704, https://doi.org/10.1016/J.JCOU.2024.102704.
- [22] J.A. Onrubia-Calvo, A. Bermejo-López, S. Pérez-Vázquez, B. Pereda-Ayo, J. A. González-Marcos, J.R. González-Velasco, Applicability of LaNiO3-derived catalysts as dual function materials for CO2 capture and in-situ conversion to methane, Fuel 320 (2022) 123842, https://doi.org/10.1016/J.FUEL.2022.123842.
- [23] L. Liu, Z. Zhang, S. Das, S. Xi, S. Kawi, LaNiO3 as a precursor of Ni/La2O3 for reverse water-gas shift in DBD plasma: effect of calcination temperature, Energy Convers. Manag 206 (2020) 112475, https://doi.org/10.1016/J. ENCONMAN.2020.112475.
- [24] K.H. Lin, C.Bin Wang, S.H. Chien, Catalytic performance of steam reforming of ethanol at low temperature over LaNiO3 perovskite, Int J. Hydrog. Energy 38 (2013) 3226–3232, https://doi.org/10.1016/J.IJHYDENE.2013.01.005.
- [25] X. Yao, X. Zhang, R. Liu, C. Pei, Z.J. Zhao, J. Gong, Oxygen activity regulation over LaNiO3 perovskites by ti substitution for chemical looping partial oxidation of methane, Chem. Eng. Sci. 278 (2023) 118911, https://doi.org/10.1016/J. CES.2023.118911.
- [26] Q. Jiang, Y. Cao, X. Liu, H. Zhang, H. Hong, H. Jin, Chemical looping combustion over a lanthanum nickel Perovskite-Type oxygen carrier with facilitated O2– transport, Energy Fuels 34 (2020) 8732–8739, https://doi.org/10.1021/acs. energyfuels.0c01038.
- [27] M. de Santana Santos, R. Frety, L. Lisi, S. Cimino, S. Teixeira Brandão, LaNi1-xCoxO3 perovskites for methane combustion by chemical looping, Fuel 292 (2021) 120187, https://doi.org/10.1016/J.FUEL.2021.120187.
- [28] S.Z. Abbas, C. de Leeuwe, A. Amieiro, S. Poulston, V. Spallina, Experimental assessment of reverse water gas shift integrated with chemical looping for lowcarbon fuels, J. CO2 Util. 83 (2024) 102775, https://doi.org/10.1016/J. JCOU.2024.102775.
- [29] M.L.T. Triviño, N.C. Arriola, Y.S. Kang, J.G. Seo, Transforming CO2 to valuable feedstocks: emerging catalytic and technological advances for the reverse water gas shift reaction, Chem. Eng. J. 487 (2024) 150369, https://doi.org/10.1016/J. CEL 2024 150369.
- [30] Y.A. Daza, D. Maiti, R.A. Kent, V.R. Bhethanabotla, J.N. Kuhn, Isothermal reverse water gas shift chemical looping on La0.75Sr0.25Co(1—Y)FeYO3 perovskite-type

- oxides, Catal. Today 258 (2015) 691–698, https://doi.org/10.1016/J.
- [31] M.M. Hossain, H.I. de Lasa, Chemical-looping combustion (CLC) for inherent CO2 separations—a review, Chem. Eng. Sci. 63 (2008) 4433–4451, https://doi.org/ 10.1016/J.CES.2008.05.028.
- [32] A. Antzara, E. Heracleous, A.A. Lemonidou, Improving the stability of synthetic CaO-based CO2 sorbents by structural promoters, Appl. Energy 156 (2015) 331–343, https://doi.org/10.1016/J.APENERGY.2015.07.026.
- [33] X. Ma, J. Liu, Y. Yang, Experimental and theoretical studies on the reactivity and reaction mechanism of LaMnO3 with CO in chemical looping combustion, J. Energy Inst. 112 (2024) 101462, https://doi.org/10.1016/J.JOEI.2023.101462.
- [34] A.J. Najfach, C.B. Almquist, R.E. Edelmann, Effect of manganese and zeolite composition on zeolite-supported Ni-catalysts for dry reforming of methane, Catal. Today 369 (2021) 31–47, https://doi.org/10.1016/J.CATTOD.2020.07.058.
- [35] F. Hildor, T. Mattisson, C. Linderholm, H. Leion, Metal impregnation on steel converter slag as an oxygen carrier, Greenhouse Gases Science Technology 13 (2023) 509–519, https://doi.org/10.1002/GHG.2202.
- [36] Q. Jiang, Y. Cao, X. Liu, H. Zhang, H. Hong, H. Jin, Chemical looping combustion over a lanthanum nickel Perovskite-Type oxygen carrier with facilitated O2– transport, Energy Fuels 34 (2020) 8732–8739, https://doi.org/10.1021/acs. energyfuels.001038.
- [37] Federico Russo, Kinetic modeling of CO 2 splitting reactions using perovskites in chemical looping for syngas production, Master's Dissertation, Politecnico di Torino, 2021. (https://webthesis.biblio.polito.it/17441/) (accessed May 16, 2025)
- [38] A. Zaidi, C. de Leeuwe, S. Chansai, C. Hardacre, A. Garforth, C. Parlett, V. Spallina, Development of iron-nickel containing perovskites with increased oxygen carrier capacity for chemical looping H2 production, J. Environ. Chem. Eng. 13 (2025) 115069, https://doi.org/10.1016/J.JECE.2024.115069.
- [39] W. Ding, K. Zhao, S. Jiang, Z. Zhao, Y. Cao, F. He, Alkali-metal enhanced LaMnO3 perovskite oxides for chemical looping oxidative dehydrogenation of ethane, Appl. Catal. A Gen. 609 (2021) 117910, https://doi.org/10.1016/J. APCATA 2020.117210
- [40] Z. Gu, K. Li, H. Wang, S. Qing, X. Zhu, Y. Wei, X. Cheng, H. Yu, Y. Cao, Bulk monolithic Ce–Zr–Fe–O/Al2O3 oxygen carriers for a fixed bed scheme of the chemical looping combustion: reactivity of oxygen carrier, Appl. Energy 163 (2016) 19–31, https://doi.org/10.1016/J.APENERGY.2015.10.177.
- [41] G. Yang, H. Yu, X. Huang, F. Peng, H. Wang, Effect of calcium dopant on catalysis of Ir/La2O3 for hydrogen production by oxidative steam reforming of glycerol, Appl. Catal. B 127 (2012) 89–98, https://doi.org/10.1016/J. APCATB.2012.08.003.
- [42] R.B. Kamble, N. Tanty, A. Patra, V. Prasad, Field emission properties and strong localization effect in conduction mechanism of nanostructured perovskite LaNiO3, Appl. Phys. Lett. 109 (2016) 083102, https://doi.org/10.1063/1.4961312.
- [43] A. Akhtar, K. Akram, Z. Aslam, I. Ihsanullah, N. Baig, M.M. Bello, Photocatalytic degradation of p-nitrophenol in wastewater by heterogeneous cobalt supported ZnO nanoparticles: modeling and optimization using response surface methodology, Environ. Prog. Sustain Energy 42 (2023) e13984, https://doi.org/ 10.1003/9312024
- [44] F. Zhu, Y. Gao, J. Ding, J. Qiu, Synergistic enhancement of the near-infrared luminescence properties of ni 2+-doped SrTiO 3 perovskite phosphors and their application, J. Mater. Chem. C. Mater. 11 (2023) 10236–10246.
- [45] B. Dou, L. Zhao, H. Zhang, K. Wu, H. Zhang, Renewable hydrogen production from chemical looping steam reforming of biodiesel byproduct glycerol by mesoporous oxygen carriers, Chem. Eng. J. 416 (2021) 127612, https://doi.org/10.1016/J. CFJ.2020.127612.
- [46] A. Das, A.C. Mandal, S. Roy, P.M. Nambissan, Mn-doping in NiO nanoparticles: defects-modifications and associated effects investigated through positron annihilation spectroscopy, J. Nanosci. Nanotechnol. 16 (2016) 4153–4163.
- [47] D. Cui, Y. Qiu, Y. Lv, M. Li, S. Zhang, N. Tippayawong, D. Zeng, R. Xiao, A high-performance oxygen carrier with high oxygen transport capacity and redox stability for chemical looping combustion, Energy Convers. Manag. 202 (2019) 112209, https://doi.org/10.1016/J.ENCONMAN.2019.112209.
- [48] I. Samprón, F. García-Labiano, M.T. Izquierdo, L.F. de Diego, Understanding the structural changes on Fe2O3/Al2O3 oxygen carriers under chemical looping gasification conditions, Fuel 355 (2024) 129326, https://doi.org/10.1016/J. EUEL 2023 129326
- [49] A. Abdalla, M. Mohamedali, N. Mahinpey, Recent progress in the development of synthetic oxygen carriers for chemical looping combustion applications, Catal. Today 407 (2023) 21–51, https://doi.org/10.1016/J.CATTOD.2022.05.046.
- [50] T. Götsch, L. Schlicker, M.F. Bekheet, A. Doran, M. Grünbacher, C. Praty, M. Tada, H. Matsui, N. Ishiguro, A. Gurlo, B. Klötzer, S. Penner, Structural investigations of La0.6Sr0.4FeO3-δ under reducing conditions: kinetic and thermodynamic limitations for phase transformations and iron exsolution phenomena, RSC Adv. 8 (2018) 3120-3131, https://doi.org/10.1039/C7RA12309D.
- [51] A. Zaidi, C. de Leeuwe, V. Spallina, Bi-metallic Ni–Fe LSF perovskite for chemical looping hydrogen application, Powder Technol. 436 (2024) 119510, https://doi. org/10.1016/J.POWTEC.2024.119510.
- [52] V. Manovic, J.P. Charland, J. Blamey, P.S. Fennell, D.Y. Lu, E.J. Anthony, Influence of calcination conditions on carrying capacity of CaO-based sorbent in CO2 looping cycles, Fuel 88 (2009) 1893–1900, https://doi.org/10.1016/J.FUEL.2009.04.012.
- [53] S.A. Salaudeen, B. Acharya, A. Dutta, CaO-based CO2 sorbents: a review on screening, enhancement, cyclic stability, regeneration and kinetics modelling, J. CO2 Util. 23 (2018) 179–199, https://doi.org/10.1016/J.JCOU.2017.11.012.

- [54] B. González, G.S. Grasa, M. Alonso, J.C. Abanades, Modeling of the deactivation of CaO in a carbonate loop at high temperatures of calcination, Ind. Eng. Chem. Res 47 (2008) 9256–9262, https://doi.org/10.1021/ie8009318.
- [55] S.Z. Abbas, J.R. Fernández, A. Amieiro, M. Rastogi, J. Brandt, V. Spallina, Lab-scale experimental demonstration of CaCu chemical looping for hydrogen production and in-situ CO2 capture from a steel-mill, Fuel Process. Technol. 237 (2022) 107475, https://doi.org/10.1016/J.FUPROC.2022.107475.
- [56] M.A. Naeem, A. Armutlulu, Q. Imtiaz, F. Donat, R. Schäublin, A. Kierzkowska, C. R. Müller, Optimization of the structural characteristics of CaO and its effective stabilization yield high-capacity CO2 sorbents, Nat. Commun. 9 (2018) 2408, https://doi.org/10.1038/s41467-018-04794-5.
- [57] P. Teixeira, C. Bacariza, I. Mohamed, C.I.C. Pinheiro, Improved performance of modified CaO-Al2O3 based pellets for CO2 capture under realistic Ca-looping conditions, J. CO2 Util. 61 (2022) 102007, https://doi.org/10.1016/J. JCOU.2022.102007.
- [58] J. Chen, P.C. Hayes, Mechanisms and kinetics of reduction of solid NiO in CO/CO2 and CO/Ar gas mixtures, Metall. Mater. Trans. B 50 (2019) 2623–2635, https://doi.org/10.1007/s11663-019-01662-5.
- [59] L. Gómez, I. Martínez, G. Grasa, R. Murillo, Different feed mixtures for the Sorption-Enhanced methanation (SEM) process on a Lab-Scale TRL-3 Fixed-Bed reactor, Energy Fuels 38 (2024) 17834–17846, https://doi.org/10.1021/acs. congressively-403633
- [60] A. Shekari, R. Labrecque, G. Larocque, M. Vienneau, M. Simoneau, R. Schulz, Conversion of CO2 by reverse water gas shift (RWGS) reaction using a hydrogen oxyflame, Fuel 344 (2023) 127947, https://doi.org/10.1016/J. FUEL 2023 127947
- [61] D.J. Deka, S. Gunduz, T. Fitzgerald, J.T. Miller, A.C. Co, U.S. Ozkan, Production of syngas with controllable H2/CO ratio by high temperature co-electrolysis of CO2 and H2O over ni and Co- doped lanthanum strontium ferrite perovskite cathodes, Appl. Catal. B 248 (2019) 487–503, https://doi.org/10.1016/J.
- [62] S.Z. Abbas, C. de Leeuwe, A. Amieiro, S. Poulston, V. Spallina, Experimental assessment of reverse water gas shift integrated with chemical looping for lowcarbon fuels, J. CO2 Util. 83 (2024) 102775, https://doi.org/10.1016/J. ICOL 2024 102775
- [63] A. Zaidi, C. de Leeuwe, Y. Yan, M. Fella, W. Hu, I.S. Metcalfe, V. Spallina, Experimental investigation of La0.6Sr0.4FeO3 -8 pellets as oxygen carriers for chemical-looping applications, Int J. Hydrog. Energy 94 (2024) 535–544, https://doi.org/10.1016/J.IJHYDENE.2024.10.404.
- [64] P.C. Kuo, Z. Sun, F. Özdemir, M. Aziz, W. Wu, CO2 utilization in chemical looping gasification and co-gasification of lignocellulosic biomass components over ironbased oxygen carriers: thermogravimetric behavior, synergistic effect, and reduction characteristics, J. Environ. Chem. Eng. 11 (2023) 109971, https://doi. org/10.1016/J.JECE.2023.109971.

- [65] D. Kang, H.S. Lim, M. Lee, J.W. Lee, Syngas production on a Ni-enhanced Fe2O3/ Al2O3 oxygen carrier via chemical looping partial oxidation with dry reforming of methane, Appl. Energy 211 (2018) 174–186, https://doi.org/10.1016/J. APPNERGY 2017 11 018
- [66] D. Wang, L. Jin, Y. Li, B. Wei, D. Yao, H. Hu, Upgrading of vacuum residue with chemical looping partial oxidation over Fe-Mn mixed metal oxides, Fuel 239 (2019) 764–773, https://doi.org/10.1016/j.fuel.2018.11.070.
- [67] H.M. Ansari, A.S. Bass, N. Ahmad, V.I. Birss, Unraveling the evolution of exsolved Fe–Ni alloy nanoparticles in Ni-doped La0.3Ca0.7Fe0.7Cr0.3O3–δ and their role in enhancing CO2–CO electrocatalysis, J. Mater. Chem. A Mater. 10 (2022) 2280–2294, https://doi.org/10.1039/D1TA07552G.
- [68] D.-K. Lee, K. Fykouras, T. Kodalle, R.F. Moral, C.P. Schwartz, N. Tamura, K. V. Lawler, L. Leppert, C.M. Sutter-Fella, Strain engineering: reduction of microstrain at the perovskite surface via alkali metal chloride treatment enhances stability, ACS Energy Lett. 10 (2025) 1039–1049, https://doi.org/10.1021/acsenergylett.4c03334.
- [69] V.D. Mote, Y. Purushotham, B.N. Dole, Williamson-Hall analysis in estimation of lattice strain in nanometer-sized ZnO particles, J. Theor. Appl. Phys. 6 (2012) 6, https://doi.org/10.1186/2251-7235-6-6.
- [70] R. Molinder, T.P. Comyn, N. Hondow, J.E. Parker, V. Dupont, In situ X-ray diffraction of CaO based CO2 sorbents, Energy Environ. Sci. 5 (2012) 8958–8969, https://doi.org/10.1039/C2EE21779A.
- [71] D. Wu, J.-M. Commenge, E. Fort, C. Hardy, J. Pecquery, L. Falk, Performance, efficiency, and flexibility analysis of a High-Temperature proton exchange membrane fuel Cell-Based Micro-Combined Heat-and-Power system with intensification of the steam methane reforming step by using a millistructured reactor, ACS Omega 8 (2023) 20589–20610, https://doi.org/10.1021/acsomega.3c01143.
- [72] P.D. Cavaliere, A. Perrone, A. Silvello, Water electrolysis for the production of hydrogen to be employed in the ironmaking and steelmaking industry, Metals 11 (2021), https://doi.org/10.3390/met11111816.
- [73] L. Fei, H. Sun, Y. Li, Y. Gu, W. Zhou, Z. Shao, Recent advances in innovative systems for electrocatalytic hydrogen production, Energy Environ. Sci. 18 (2025) 6456–6529, https://doi.org/10.1039/D4EE03084B.
- [74] B. Bulfin, M. Zuber, O. Gräub, A. Steinfeld, Intensification of the reverse water–gas shift process using a countercurrent chemical looping regenerative reactor, Chem. Eng. J. 461 (2023) 141896, https://doi.org/10.1016/J.CEJ.2023.141896.
- [75] Y. Yan, R.J. Lee Pereira, M. Fella, Z. Li, W. Hu, Y. Larring, I.S. Metcalfe, Experimental investigation of La0.6Sr0.4FeO3-8 pellets as oxygen carriers in a counter-current packed-bed reactor for efficient chemical looping CO2 splitting, J. CO2 Util. 88 (2024) 102935, https://doi.org/10.1016/J.JCOU.2024.102935.
- [76] I.S. Metcalfe, B. Ray, C. Dejoie, W. Hu, C. de Leeuwe, C. Dueso, F.R. García-García, C.-M. Mak, E.I. Papaioannou, C.R. Thompson, J.S.O. Evans, Overcoming chemical equilibrium limitations using a thermodynamically reversible chemical reactor, Nat. Chem. 11 (2019) 638–643, https://doi.org/10.1038/s41557-019-0273-2.